# Harnessing Photoelectrochemistry for Wastewater Nitrate Treatment Coupled with Resource Recovery

Luisa Barrera[1] and Rohini Bala Chandran[1*]

Abstract

Wastewater is a misplaced resource well suited to recover nutrients, value-added chemicals, energy, and clean water. A photoelectrochemical device is proposed to transform wastewater nitrates to ammonia and nitrous oxide, coupled with water oxidation. Numerical models were developed to quantify the dependence of process efficiencies and nitrogen-removal rates on light absorber band gaps, electrocatalytic kinetic parameters, competing oxygen reduction and hydrogen evolution reactions, and the reacting nitrate species concentrations that affect the mass-transfer limited current densities. With a single light-absorber and state-of-the-art catalysts, optimal solar-to-chemical efficiencies of 7% and 10% and nitrogen-removal rates of 260 and 395 g_N m^{-2} day^{-1} are predicted for nitrate reduction to ammonia and nitrous oxide respectively. The influence of competing reactions on the performance depends on the nitrate concentration and band gap of the light absorber modeled. Oxygen reduction is more dominant than hydrogen evolution to compete with the nitrate reduction reaction, but is mass-transfer limited. Even with kinetic parameters that enhanced the driving forces for the competing reactions, the performance is only minimally affected by these reactions for optimally selected band gaps and nitrate concentrations larger than 100 mM. Theoretically predicted peak nitrogen removal rates and specific energy intensities are competitive with reported estimates for bioelectrochemical and Sharon-Anammox processes for ammonia recovery and nitrogen removal respectively. This result, together with the added benefit of harnessing sunlight to produce value-added products, indicates promise in the photoelectrochemical approach as a tertiary pathway to recover nutrients and energy from wastewater nitrates.

TOC Graphic
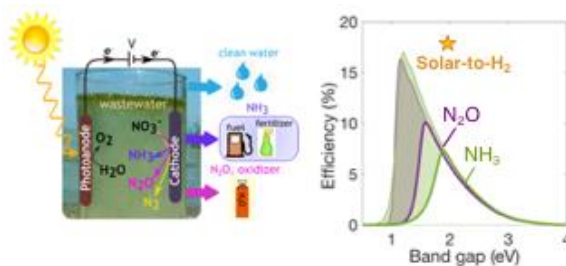
[1] Department of Mechanical Engineering, 2350 Hayward St., G. G. Brown Building, University of Michigan, Ann Arbor, MI 48109
[*]Corresponding author: rbchan@umich.edu

1. Introduction

Excessive anthropogenic production of nitrogen fertilizers combined with fossil-fuel combustion has significantly disrupted the natural nitrogen cycle[1–3], leading to the contamination of groundwater and other surface-water bodies with various reactive forms of nitrogen—nitrates (NO_3^-), nitrites (NO_2^-), ammonia (NH_3), ammonium (NH_4^+) and organic nitrogen. These contaminants result in environmental threats such as algal blooms, suffocation of aquatic wildlife, and health risks in humans, e.g. excessive amounts of nitrates in drinking water causes methemoglobinemia ("blue baby" syndrome)[4–8]. While several strategies have been reported to recover value-added products — energy from biogas and chemicals including biopolymers, bio-oils, and biochar from organic contaminants — far less emphasis has been placed on nutrient (i.e. nitrogen) and energy recovery from nitrogen contaminants[9–12].

This study focuses on evaluating the feasibility of a photoelectrochemical approach to recover nitrogen nutrients from NO_3^- contaminants present in ion-exchange brines[13–16] and treated wastewater[11,17–19]. Biological nitrification-denitrification treatment processes are attractive as they utilize microbes to consume and remove the excess nutrients[20,21]. However, these processes are energy intensive[22], not effective in effluent streams that harbor conditions unsuitable for microbial growth[3,23], and have not been optimized for resource recovery[12]. Ion-exchange[5,24,25], electrodialysis[26,27], and reverse osmosis[28,29] are used to treat nitrates (and other ions) at an industrial scale for drinking water applications, but result in the production of a secondary nitrate-concentrated brine that requires further treatment[30]. Hence, there is an increasing demand to develop wastewater treatment technologies to harness renewable energy, to be effective for a wide range of effluent stream conditions and to facilitate resource recovery in the form of nutrients and energy. To meet these critical needs, photoelectrochemical devices offer the potential to couple

sunlight with electron-transfer reactions to treat and transform nitrogen-contaminants to value-added chemicals and therefore facilitate nitrogen recovery.
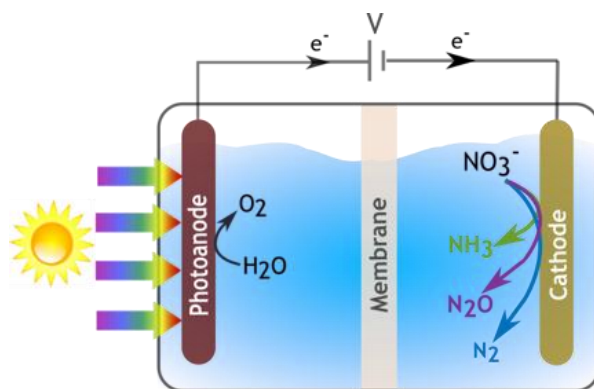
Prior work has provided theoretical limits for the solar-to-fuel energy conversion efficiencies and established guidelines to select semiconductor and co-catalysts/electrocatalysts to optimize the efficiency for photoelectrochemical water splitting devices, which generate hydrogen and oxygen from water using light absorbers and electrocatalysts[31–42]. However, the same extent of understanding is not available for photoelectrochemical nitrate treatment devices. Photocatalytic nitrate reduction has been investigated predominantly with TiO_2-based light absorbers with NO_3^- reduction often paired with sacrificial hole-scavengers (methanol, oxalic acid, and formic acid)[43–46]. However, TiO_2 limits process efficiencies due to the low sunlight absorption and the presence of hole-scavengers lead to toxicity concerns for water treatment applications. Comprehensive reviews have been reported on electrochemical denitrification, i.e. NO_3^- to N_2 conversion, including investigations on metallic and bimetallic electrocatalysts for NO_3^- to N_2 and NH_3 conversion, and studies that probe fundamental reaction mechanisms[47–60]. However, the focus in a majority of these studies has been on electrocatalytically reducing NO_3^- to N_2, which poses formidable kinetic (reactivity and selectivity) challenges. Therefore, there is a lack of knowledge on the ideal performance limits and the impacts of materials parameters on the performance of a photoelectrochemical approach to recover nitrogen nutrients from wastewater.

The objective of this study is to theoretically predict the solar-to-chemical energy conversion efficiencies and the rate of recovery of nitrogen for a photoelectrochemical device that is operating on treated wastewater with predominantly nitrate contaminants (Figure 1). A notable innovation introduced in the modeling approach developed is the capability to account for the effects of competing hydrogen evolution and the oxygen reduction reactions that can compete with

1 the desired nitrate reduction reaction at the cathode, within a simplified, yet powerful, equivalent

2 circuit modeling framework. The model developed is used to obtain the impacts of material

3 parameters, including the light-absorber band gaps, electrocatalyst exchange current densities and

4 charge-transfer coefficients for the desired and the competing reactions, and operating nitrate

5 concentration in the waste stream, on all the performance metrics. These results are interpreted to

6 provide guidelines to select materials for the light absorbers and electrocatalysts to maximize

7 resource (nitrogen) recovery. Furthermore, the predicted performance metrics are used to compare

8 the proposed approach with the state-of-the-art nitrogen removal/recovery technologies – the

9 Sharon-Annamox process[61,62] and ammonia stripping using electrochemical flow reactors[63].

10 **2. Photoelectrochemical Device for Wastewater Nitrate Treatment**

11   In this work, we propose a photoelectrochemical device to pair water oxidation with nitrate

12 reduction (Figure 1). A photoactive semiconductor anode absorbs incident sunlight and is

13 electrically connected to the cathode. The holes generated at the photoanode surface effect the

14 oxygen evolution reaction (OER) while at the cathode surface the electrons effect the nitrate

15 reduction reaction (NO3RR) to the desired products including NH_3/NH_4^+ and N_2O. An ion-

16 exchange membrane may be present to facilitate ion transport while preventing gas crossover

17 between the electrodes. Compared to the removal of NO_3^- contaminants as N_2, the transformation

18 to NH_3/NH_4^+ and N_2O recovers the N-nutrients and upgrades the *energetic value* of the reactive-

19 nitrogen contaminant species. Aqueous NH_3/NH_4^+ can be reused as a fertilizer and/or oxidized to

20 generate electricity in an ammonia fuel-cell, and gaseous NH_3 can be used as a fuel to generate

21 heat and produce electricity[64–66]. Despite being a potent greenhouse gas, N_2O is also a powerful

22 oxidizer, especially for the combustion of rocket-fuel and biogas and for supercharging

23 applications[67,68]. It increases the energy released during the combustion of CH_4 by 37% as

Oxidation		Reduction	
$2\ OH^- \rightarrow \frac{1}{2}O_2(g) + H_2O + 2e^-$	$E^0 = 1.23\ V$	$NO_3^- + 7\ H_2O + 8\ e^- \rightarrow NH_3(g) + 9\ OH^-$	$E^0 = 0.82\ V$
Net Reaction, R1:	**$NO_3^- + 3\ H_2O \rightarrow NH_3\ (g) + OH^- + 2\ O_2\ (g)$**		**$E^0_{R1} = -0.41\ V$**
$2\ OH^- \rightarrow \frac{1}{2}O_2(g) + H_2O + 2e^-$	$E^0 = 1.23\ V$	$2\ NO_3^- + 5\ H_2O + 8\ e^- \rightarrow N_2O(g) + 10\ OH^-$	$E^0 = 1.12\ V$
Net Reaction, R2:	**$2\ NO_3^- + H_2O \rightarrow N_2O\ (g) + 2\ OH^- + 2\ O_2\ (g)$**		**$E^0_{R2} = -0.11\ V$**
$2\ OH^- \rightarrow \frac{1}{2}O_2(g) + H_2O + 2e^-$	$E^0 = 1.23\ V$	$2\ NO_3^- + 6\ H_2O + 10\ e^- \rightarrow N_2(g) + 12\ OH^-$	$E^0 = 1.25\ V$
Net Reaction, R3:	**$2\ NO_3^- + H_2O \rightarrow N_2\ (g) + 2\ OH^- + 5/2\ O_2\ (g)$**		**$E^0_{R3} = 0.02\ V$**

Figure 1: Schematic of a photoelectrochemical device for treating wastewater nitrate contaminants. Selective water oxidation at the photoanode and the NO_3^- reduction pathways to form NH_3 (R1), N_2O (R2) and N_2 (R3) are depicted. All the standard potentials, E^0, for aqueous solutions at 25°C are reported vs. NHE based on a 1 atm standard state for H_2. Unless otherwise mentioned all species are in the aqueous phase[69,70]. A negative E^0 for a net reaction indicates that it is thermodynamically uphill, while a positive E^0 indicates reaction spontaneity.

1   compared to using O_2 as an oxidizer, and therefore has been previously considered as a viable end-

2   product for energy recovery[67,71].

3   As an idealized starting point for our analyses, we assumed the presence of predominantly

4   NO_3^- contaminants in the waste stream. Such an assumption could be reasonable for a tertiary

5   treatment process designed for resource recovery from nitrogen-contaminants in pre-treated

6   wastewater from municipal wastewater treatment plants, ion-exchange brines and other industrial

7   processes[11,13–19].

3. Theory & Numerical Model

A zero-dimensional (0-D), equivalent circuit model was developed to determine operating current densities and potentials, where the semiconductor light absorber was modeled as an ideal diode in series with the electrochemical reactions, which were modeled as variable resistors to account for the electrocatalyst current-overpotential behavior[31–38] (Figure 1). A nomenclature of symbols is included in the ESI. For the electrochemical reactions, kinetic and the mass-transfer potential losses were considered. While selective oxidation of water (OER) was assumed to occur at the anode (Eq.(1a)), non-selective reduction reactions were modeled at the cathode by considering parallel current pathways and by enforcing potential equality (Eq. (1a)) in the parallel branches; the overall operating potential of the diode is given by Eq. (2).

$$V_{\text{anode}} = E_{\text{eq,OER}} + \eta_{\text{OER}} \tag{1a}$$

$$V_{\text{cathode}} = \begin{cases} E_{\text{eq,NO3RR}} + \eta_{\text{NO3RR}} \\ E_{\text{eq,HER}} + \eta_{\text{HER}} \\ E_{\text{eq,ORR}} + \eta_{\text{ORR}} \end{cases} \tag{1b}$$

$$V_{\text{op}} = V_{\text{anode}} - V_{\text{cathode}} \tag{2}$$

At the anode, selective OER is justified by the low likelihood of oxidizing nitrogen-products (N_2O and NH_3 especially for pH>12[23,72]). However, at the cathode, in addition to the desired nitrate reduction reaction (NO3RR), competing hydrogen evolution (HER) and oxygen reduction (ORR) reactions were also modeled. The HER has been reported to compete with the NO3RR in prior work with Cu catalysts[3,57,72]; the ORR was considered due to the O_2 produced at the anode, which can crossover and react at the cathode surface.

The Nernstian potential, E_{eq}, was included (Eq. (3)) as the minimum electrical load at the cathode and the anode.

$$E_{\text{eq}} = E^0 + \frac{R\,T}{n_e\,F}\ln\left(\frac{a_O^{v_O}}{a_R^{v_R}}\right) \tag{3}$$
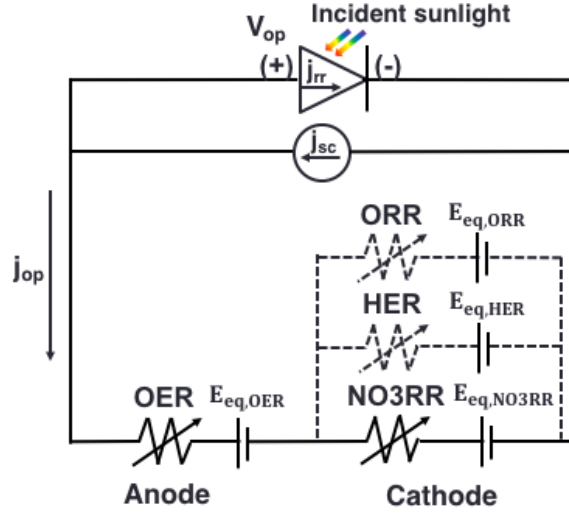
6

Figure 2: Equivalent circuit diagram to model the operation and performance of the photoelectrochemical device in Figure 1. The semiconductor light-absorber was modeled as a photodiode and the electrochemical reactions as variable resistors with minimum electrical loads corresponding to the thermodynamic potentials for the corresponding reactions. Selective oxygen evolution reaction (OER) at the anode and parallel reactions were modeled at the cathode including the desired NO3RR, and the competing HER and ORR. Desired reactions in the circuit are indicated by the solid lines and the undesired and competing reactions at the cathode are indicated by the dashed lines.

Current conservation, Eq. (4), was satisfied in the circuit, while taking into account the parallel and competing reactions occurring at the cathode. The sign convention adopted implements the reduction current densities to be negative and the oxidation current density to be positive.

$$j_{op} = j_{OER} = -\sum_{i=NO3RR,ORR,HER} j_i \tag{4}$$

Light Absorber: The semiconductor light absorber was modeled as a diode with the pertinent governing equations and key assumptions summarized in Table 1[31–38]. Ideal diode behavior with only radiative recombination (Eqs. (5)-(7)) and a large optical path length was assumed to keep the analyses general and to analyze a wide range of light absorber bandgaps. However, the trends predicted for the impacts of the material band gaps on the performance metrics are expected to be valid even with more realistic recombination models.

7

1 **Table 1**: List of the governing equations for the semiconductor light absorber in the equivalent
2 circuit (0-D) model
3

Physics modeled	Governing equations and key assumptions
Current-potential behavior of the semiconductor	Shockley-Queisser detailed-balance model[36] $$j_{\text{op}} = j_{\text{sc}} - j_{\text{rr}} \left(e^{\frac{q_e V_{\text{op}}}{n_d \, k_{\text{B}} \, T}} - 1 \right) \tag{5}$$ *(i)* Optically thick semiconductor absorbs all the above-band-gap photons to ensure that current density is not limited by the material design, i.e. planar electrodes[36], photocatalytic particle suspension reactors[33], nanowires[73] etc. *(ii)* Negligible optical losses due to reflection at the surface of the light absorber to keep the analysis generic and applicable over a wide range of material bandgaps *(iii)* Ideal diode with only radiative recombination dictated by the rate of thermal emission of photon at ambient temperature, $T = 298.15$ K
Short-circuit current density, j_{sc}	$$j_{\text{sc}} = q_e \int_{\upsilon_{\text{g}} = \frac{E_g}{k_{\text{B}} T}}^{\infty} \phi_{\text{solar}}(\upsilon) \, d\upsilon \tag{6}$$ *(i)* Electron-hole (e^-/h^+) pairs are generated by each and every incident photon with energy larger than its band gap of E_g *(ii)* Excited-state charge carriers rapidly thermalize to the band edges and each absorbed photon produces only one e^-/h^+ pair
Radiative recombination current density, j_{rr}	$$j_{\text{rr}} = 2 \, q_e \left(\frac{2\pi}{c^2} \right) \int_{\upsilon_{\text{g}}}^{\infty} \frac{\upsilon^2}{e^{\frac{h \upsilon}{k_{\text{B}} T}} - 1} \, d\upsilon \tag{7}$$ *(i)* Light absorber is surrounded by a blackbody at the same temperature as that of the diode that is at $T = 298.15$ K [36]

4   *Electrochemical Reactions*: Potential losses for the electrochemical reactions included the

5 mass-transfer ($\eta_{i,\text{mt}}$) and the kinetic ($\eta_{i,\text{k}}$) overpotentials for all the redox reactions considered, i.e.

6 i = OER, NO3RR, HER, and ORR (Eqs. (8) and (9)).

$$\eta_i = \eta_{i,\text{k}} + \eta_{i,\text{mt}} \tag{8}$$

7 The mass-transfer overpotential was included to account for the bulk concentration-dependent

8 limiting current densities for all redox species (NO_3^-/NO_2^- for NO3RR, H_2O/H_2 for HER, and

9 O_2/OH for ORR) except for the OER. For the OER, this mass-transfer overpotential component in

10 Eq. (8) is assumed to be negligibly small because of the large concentration of the reacting species,

11 $c_{H_2O} = 55.5$ M (pH = 1) and $c_{OH^-} = 1$ M (pH = 14). Equation (9) accounts for the mass-transfer

12 overpotential,

$$\eta_{i,\text{mt}} = \frac{R\,T}{F\,n_e} \ln\left(\frac{\left(1 - \frac{j_i}{j_{l,i,c}}\right)^{\nu_{i,c}}}{\left(1 - \frac{j_i}{j_{l,i,a}}\right)^{\nu_{i,a}}}\right) \tag{9}$$

1 where, j_l is the limiting current density for the cathodic (c) and anodic (a) half-reactions. Limiting

2 current densities were calculated assuming diffusion-limited species transport (Eq. (10)) of the

3 oxidized (O) or reduced species (R), with a concentration boundary layer thicknesses of 10 µm,

4 $\delta_{BL} = 10$ µm, which is a reasonable assumption for planar electrode architectures with laminar

5 flow regime[74],

$$j_{l,i,a/c} = \pm \frac{n_e\,F\,D_{R/O}\,C_{R/O}}{\delta_{BL}\,\nu_{R/O}} \tag{10}$$

6
7 Butler-Volmer equations were applied to model reversible electron transfer reactions (Eq. (11))

8 and irreversible cathodic reactions (Eq. (12)),

$$j_i = j_{0,\text{ref},i} \left(\frac{C_{R,\text{bulk}}}{C_{R,\text{bulk,ref}}}\right)^{(\nu_R\,\alpha_{c,i})/n_e} \left(\frac{C_{O,\text{bulk}}}{C_{O,\text{bulk,ref}}}\right)^{(\nu_O\,\alpha_{a,i})/n_e} \left(\exp\left(\frac{\alpha_{a,i}\,\eta_{i,k}}{R\,T/F}\right) - \exp\left(\frac{-\alpha_{c,i}\,\eta_{i,k}}{R\,T/F}\right)\right) \tag{11}$$

$$j_i = j_{0,\text{ref},i} \left(\frac{C_{O,\text{bulk}}}{C_{O,\text{bulk,ref}}}\right)^{1-\alpha_{c,i}/n_e} \left(-\exp\left(\frac{-\alpha_{c,i}\,\eta_{i,k}}{R\,T/F}\right)\right) \tag{12}$$

9 where, $j_{0,\text{ref,i}}$ is the reference surface- and concentration-dependent exchange current density of

10 the ith reaction (for a selected electrocatalyst, the larger the $j_{0,i}$ value, the faster the rate is for both

11 the anodic and cathodic directions of the reversible redox reactions); α_a and α_c are the charge-

12 transfer coefficients indicating the symmetry of the activation barrier for the reaction. Equation

13 (11) was applied to model the kinetics for OER, HER, and ORR, whereas Eq. (12) was used for

14 NO3RR. A literature review was performed to identify the state-of-the-art catalysts for OER and

15 NO3RR, based on which the kinetic parameters $(j_{0,\text{ref},i}, \alpha_{c,i}, \alpha_{a,i})$ were determined for these

16 reactions (Table 2). For NO3RR, catalysts were selected based on satisfying two criteria: (a) the

17 availability of kinetic parameters, or cyclic voltammograms or Tafel plots based on which kinetic

18 parameters can be extracted, and (b) the inclusion of product composition analyses to determine

Table 2: Reactions modeled with relevant pH, reference exchange current density, $j_{0,\text{ref}}$; charge transfer coefficients, α_c and α_a; N/A for the charge-transfer coefficients implies the use of the irreversible equation form (Eq. (12)); bulk reference concentrations, $c_{\text{bulk,ref}}$, extracted from the literature for the catalysts are listed; pH 1 and pH 14 data used for NH_3 and N_2O production respectively

Reaction	pH	Catalyst	Kinetic Parameters for Eqs. (11) and (12)			
			$j_{0,\text{ref}}$ (A m^{-2})	α_c	α_a	$c_{\text{bulk,ref}}$ (mM)
OER[33,41,75]	1	RuO$_2$	6.68×10^{-4}	0.1	1	$c_{H^+} = 1000$; $c_{O_2,\text{aq}} = 1.3$
	14	IrO$_2$	0.48	0.63	0.39	$c_{OH^-} = 1000$; $c_{O_2,\text{aq}} = 1.3$
NO3RR[57,58]	1	Sn-Pt	2.12×10^{-3}	0.54	N/A	$c_{NO_3^-} = 10$; $c_{H^+} = 100$
	14	Cu	1.12×10^{-2}	0.30	N/A	$c_{NO_3^-} = 100$; $c_{OH^-} = 1000$
HER[76,77]	1	Pt	10	0.5	0.5	$c_{H^+} = 1000$; $c_{H_2,\text{aq}} = 0.78$
	14					$c_{OH^-} = 1000$; $c_{H_2,aq} = 0.78$
ORR[78–81]	1	Pt	10^{-1}	0.9	0.1	$c_{H^+} = 100$; $c_{O_2,\text{aq}} = 1.3$
	14		10^{-5}			$c_{OH^-} = 1000$; $c_{O_2,\text{aq}} = 1.3$

the selectivity to the desired nitrate reduction products[49–51,55–58,82,83]. It was determined that Cu (pH of 14) and Sn-Pt (pH of 1) exhibited high product selectivity for the reduction of NO_3^- to NH_3 and N_2O respectively[57,58]. The kinetics for the NO3RR was modeled by considering the irreversible reduction of NO_3^- to NO_2^- as the rate-determining step[3,23].

$$NO_3^- + H_2O + 2\ e^- \rightarrow NO_2^- + 2\ OH^- \qquad E^0 = 0.835 \text{ V v/s NHE} \qquad (13)$$

Because of the high product selectivity ($> 98\%$) reported for the state-of-the-art catalysts, we assumed full selectivity in the transformation of NO_2^- to the desired products on the selected catalysts. This is a simplifying assumption to overcome the lack of mechanistic information to model the sequence of elementary steps needed for the various nitrogen-products considered in this study[3]. In the same pH conditions, the most suitable OER catalysts were identified to be IrO$_2$ (pH = 14) and RuO$_2$ (pH = 1)[33,41,75].

Modeling Competing Reactions: The electrocatalytic parameters ($j_{0,\text{ref},i}, \alpha_{c,i}, \alpha_{a,i}$) for the competing reactions (ORR and HER) at the cathode were determined such that the impact of the "*worst-case*" on the efficiency and rates of nitrogen-recovery from the products formed could be

1   investigated. The largest exchange current density, $j_{0,\text{ref},i}$, for the competing HER was based on

2   the kinetics reported for Pt at both pH = 1 and pH = 14 (Table 2). The HER was modeled to be

3   fully reversible with $\alpha_c=\alpha_a=0.5$, as justified by experimentally reported measurements for various

4   catalysts[76,84]. For the ORR, the $j_{0,\text{ref},i}$ was selected based on reported values for Pt for pH =1 and

5   14[78–81], and the ORR cathodic charge-transfer coefficient was assumed to be $\alpha_c = 0.9$ to model a

6   surface that is favorable to ORR. In the headspace of the reactor, standard atmospheric conditions

7   (1 atm, 25° C) with a mole-fraction of 20.9% of O_2, trace amounts of H_2 (0.5 ppm) and balance N_2

8   was modeled.

9   Overall, we have a consistent system of algebraic equations (up to 12 when competing

10   reactions are included) that are simultaneously solved for the variables – $j_{\text{op}}, V_{\text{op}}, \eta_{\text{OER,k}},$

11   $j_{\text{NO3RR}}, \eta_{\text{NO3RR,k}}, \eta_{\text{NO3RR,mt}}, j_{\text{HER}}, \eta_{\text{HER,k}}, \eta_{\text{HER,mt}}, j_{\text{ORR}}, \eta_{\text{ORR,k}}, \eta_{\text{ORR,mt}}.$ The   system   of

12   equations was solved using the *fsolve* function in Matlab R2018a, with a function tolerance of 10^{-4},

13   an optimality tolerance of 10^{-4}, a step tolerance of 10^{-4}, an average finite difference step size of

14   1.5×10^{-4}, and with the default solver algorithm (trust-region dogleg) or in instances when the

15   convergence was challenging, the Levenberg-Marquardt algorithm was applied[85].

16   *Performance Metrics:* The efficiency of converting the incident solar power (1 Sun or

17   1000 W m^{-2}) to the output chemical power was obtained using Eq. (14), where, $\dot{r}_i$ is the molar flux

18   of NH_3 and N_2O produced, and Δg_i^0 is the standard state free-energy change for the respective

19   oxidation reactions (Table 2).

$$\eta_{\text{solar-to-chemical},i} = \frac{\dot{r}_i \left| \Delta g_i^0 \right|}{1000}; i = NH_3, N_2O \tag{14}$$

20   The molar flux, $\dot{r}$, of NH_3 and N_2O (in mol m^{-2} s^{-1}) produced is related to the nitrate reduction

21   current density, $j_{\text{NO3RR}},$

$$\dot{r}_i = \frac{|j_{NO3RR}|}{n_{e,\text{tot}} F}; i = NH_3, N_2O \tag{15}$$

1 The oxidation of gaseous NH_3 with O_2 was modeled, $\Delta g^0_{NH_3/H_2O}$= -339 kJ mol^{-1}, whereas gaseous

2 N_2O was used as an oxidizer to combust CH_4, $\Delta g^0_{CH_4,N_2O/H_2O} = $ -308.7 kJ mol^{-1}. Solar energy

3 conversion efficiencies for the NO_3^--to-N_2 transformation is not reported because the N_2 produced

4 has to first be reduced to NH_3/NH_4^+ to facilitate energy recovery, and this step in itself is highly

5 energy intense[86,87]. For comparison, when solar-to-hydrogen efficiencies are computed for

6 photoelectrochemical water-splitting devices, the molar rate of H_2 production with $\Delta g^0_{H_2/H_2O} = $

7 237.4 kJ mol^{-1} is used.

8 The rate of nitrogen-removal and nitrogen-recovery, R_N (in g$_N$ m^{-2} day^{-1}) are equal and

9 directly proportional to the molar flux, $\dot{r}_i$, of the products formed from the nitrate contaminants

10 (Eq. (16)). In Eq. (16), $m_N = 14$ g, is the molar mass of atomic-nitrogen and $t_{\text{day}} = 86400$ s day^{-}

11 ^{1}. Therefore, a larger solar-to-chemical efficiency is also indicative of improved rates of nitrogen

12 removal/recovery in our analyses.

$$R_N = \dot{r}_i \, m_N t_{\text{day}}; \ i = NH_3, N_2O \tag{16}$$

13 The specific energy intensity E_N (in MJ kg$_N^{-1}$) (Eq. (17)) is a measure of the total energy required

14 per unit mass of nitrogen removed and is commonly used as a metric to compare various

15 technologies from an energy-consumption standpoint. The calculation in Eq. (17) assumed that the

16 device steadily operates at the predicted current-density, j_{op}, and operating potential, V_{op}.

17 Therefore, there is lack of dependence on current-density for the E_N calculation, as the current-

18 density term appears both in the numerator (total energy consumption) and the denominator (total

19 mass of nitrogen removed).

$$E_{\text{N}} = \frac{V_{\text{op}} \, n_e \, F}{m_{\text{N}}} \tag{17}$$

4. Results & Discussion

4.1 Composition of Nitrogen-Contaminants in Wastewater

Figure 3 shows the source-dependent variability in the composition of nutrient contaminants, including organic, nitrogen and phosphorous contaminants, for various point-sources of wastewater. Point-sources considered in this study included low-level nuclear wastes, municipal wastewater effluents, ion-exchange brines, power generation, and oil/gas and manufacturing processes. Even though diffuse sources, such as agricultural runoff streams and landfill wastewater, also cause nutrient contamination, they are not included in Figure 3 because the contaminant species and concentrations in these sources are strongly influenced by the collection strategy. Biological oxygen demand (BOD) quantifies the amount of the dissolved oxygen required to biologically oxidize the organic contaminants; therefore, the larger the BOD value, the larger the organic contaminant concentration[88]. Nitrogen-species, including NO_3^-, NO_2^-, and NH_4^+, and phosphates (PO_4^{3-}) were also considered. Whereas, nitrogen contaminants dominate in nuclear wastes (159,000 mg/L total nitrogen species), ion-exchange brines (5,270 mg/L), and power production processes (300 mg/L), organic species overshadow nutrient contaminants in municipal wastewater effluents and oil/gas processes. The concentrations of all three contaminants are comparable for effluents from manufacturing processes. In many waste streams, PO_4^{3-} contamination is comparable to the nitrogen-contamination, which indicates the potential for phosphorous-recovery from these sources. For reference, the U.S. Environmental Protection Agency (EPA) established nitrogen-contaminant levels for drinking water are 44.3 mg-NO_3^-/L and 3.3 mg-NO_2^-/L[89].
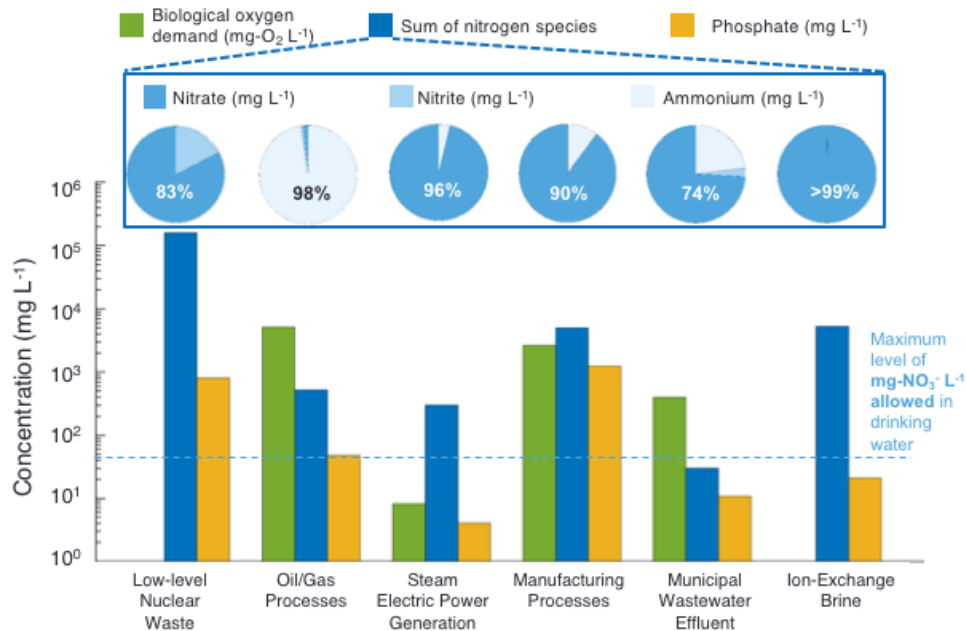
Figure 3: Concentrations of biological oxygen demand (mg-O$_2$/L), nitrogen species, and phosphate (mg-PO$_4^{3-}$/L) in different waste streams. Percentage breakdown of nitrogen species – NO$_3^-$ (mg-NO$_3^-$/L), NO$_2^-$ (mg-NO$_2^-$/L) and NH$_4^+$ (mg-NH$_4^+$/L) is indicated for each source. Data was compiled from the US Environmental Protection Agency (EPA) development documents[90,91], EPA's database for industrial wastewater treatment technologies[92], and pertinent journal papers[11,13–19,60,93–106]. EPA's specifications for nitrogen-contaminants in drinking water: < 44.3 mg-NO$_3^-$/L (dashed blue line) and < 3.3 mg-NO$_2^-$/L[89].

1 More than 80% of all nitrogen-contaminants are in the form of NO$_3^-$ in all point sources except for

2 oil/gas processes, where the NH$_4^+$ species predominates. Therefore, tertiary processes targeting

3 nitrogen recovery could be valuable in pre-treated wastewaters from these sources. Furthermore,

4 the source-dependent fluctuation in the NO$_3^-$ concentration establishes a need to quantify the

5 impacts of this variation on the predicted process efficiencies and the removal/recovery rates.

6 **4.2 Solar-to-Chemical Efficiencies and Nitrogen Removal/Recovery Rates**
7
8 Figure 4 presents the equivalent-circuit model predictions for the solar energy conversion

9 efficiencies (Eq. (14)) for NH$_3$ and N$_2$O production as a function of the semiconductor band gaps

10 and electrocatalytic parameters. A bulk NO$_3^-$ concentration of 100 mM, which is approximately

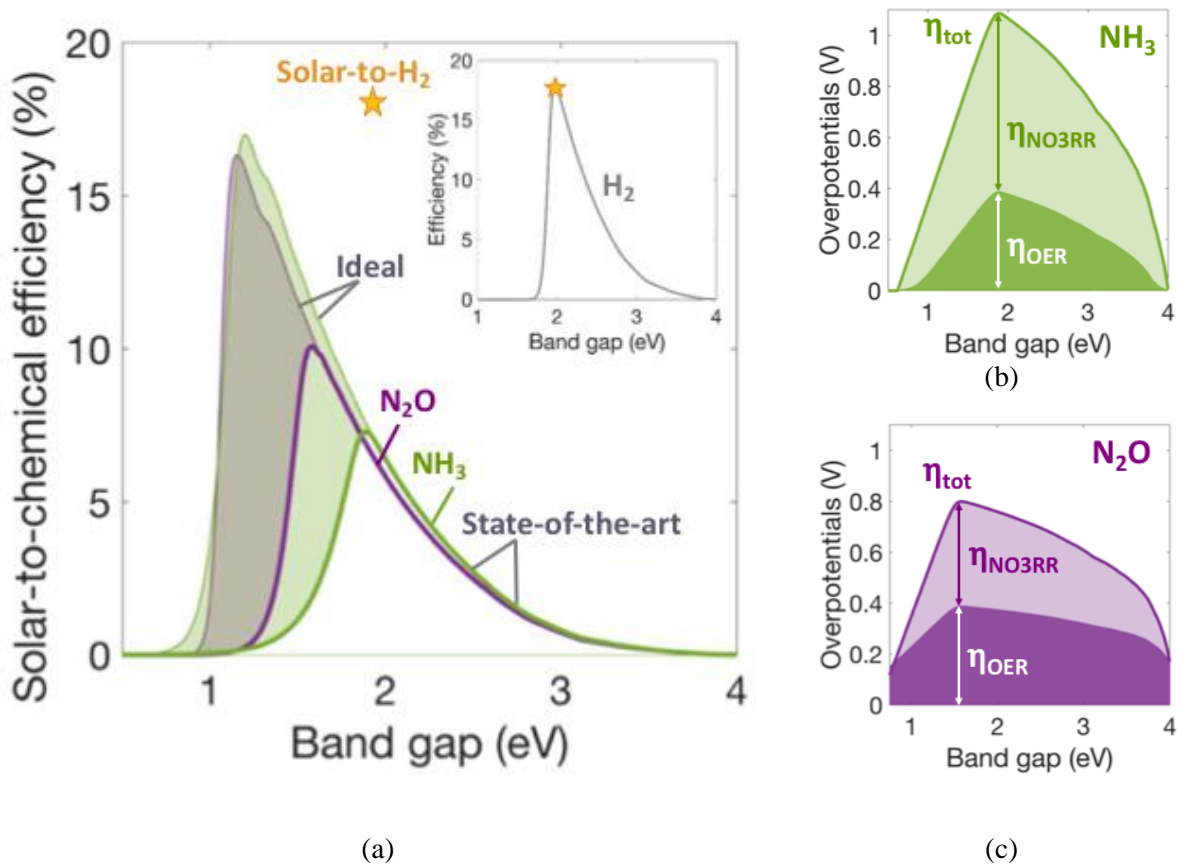11 the average of the NO$_3^-$ concentration in the point-source effluents in Figure 3, was used in these

Figure 4: (a) Solar-to-chemical energy conversion efficiencies, $\eta_{solar-to-chemical}$, for water oxidation and NO_3^- reduction to NH_3 (green) and N_2O (purple) with RuO_2, Cu (pH 14) and IrO_2, Sn-Pt (pH 1) catalysts for the OER and the NO3RR, respectively. Solar-to-hydrogen efficiency in the inset was computed for RuO_2 (OER) and Pt (HER) catalysts at pH=1; maximum solar-to-H_2 efficiency is represented as a star[38]. The thick solid lines and the thin solid lines represent efficiencies with state-of-the-art and ideal nitrate reduction catalysts. Total kinetic overpotential, η_{tot}, and the split between the oxidation (OER) overpotential, η_{OER}, (dark shaded area) and the NO3RR overpotential, η_{NO3RR}, (light shaded area) is shown for (b) NH_3 (green) and (c) N_2O (purple). Standard state potential from Eq. (3) was used and a 100 mM NO_3^- species concentration was modeled; $E^0_{NO3RR} = 0.835$ V vs NHE.

1

2 calculations, and selective OER and NO3RR was modeled to estimate the upper limits for the solar

3 energy conversion efficiencies. Irrespective of the catalytic parameters modeled, the solar-to-

4 chemical efficiency initially increases with an increase in the semiconductor band gap until an

5 optimum point, after which, the efficiency decreases. The optimum arises because of the tradeoffs

6 between the increased light absorption for the smaller band gaps and the decreased radiative

7 recombination losses for the larger band gaps. For state-of-the-art catalysts, peak solar-to-chemical

1   efficiencies are 10.1% and 7.3%, corresponding to peak nitrogen removal/recovery rates of

2   395.3 g_N m^{-2} day^{-1} and 260.3 g_N m^{-2} day^{-1}, for N_2O and NH_3 formation respectively. The trends for

3   the nitrogen removal/recovery rates are not shown in Figure 4 because they exactly match with the

4   trends obtained for the solar-to-chemical efficiencies. The higher efficiencies and recovery-rates

5   for the production of N_2O relative to NH_3 is due to the more effective catalysis for the NO3RR

6   with the Sn-Pt catalyst as compared to Cu. Therefore, at peak efficiencies, relatively smaller kinetic

7   overpotentials resulted for N_2O as compared to NH_3—412 mV v/s 689 mV for the NO3RR (Figure

8   4 (b) and (c)). *Ideal* efficiency plots were obtained by imposing rapid kinetics for the NO3RR, i.e.

9    $\eta_{red} = 0$, with state-of-the-art OER catalysts. The optimal solar-to-chemical efficiencies for the

10   *ideal* case more than double, from 7.3% to 17%, for NH_3 and increase from 10.1% to 16.3% for

11   N_2O, as compared to the *state-of-the-art* NO3RR catalysts. The solar-to-chemical efficiency for

12   N_2O formation is relatively less sensitive to the kinetic parameters modeled for NO3RR, as

13   opposed to NH_3 formation, because the OER overpotentials dominate the potential losses in the

14   former. This dramatic boost in overall performance, achieved by eliminating the nitrate-reduction

15   kinetic overpotential, indicates that effective nitrate reduction electrocatalysts can significantly

16   boost the efficiencies for any light-absorber and that the performance predictions are highly

17   sensitive to the catalytic parameters modeled. To place these efficiencies in context, Figure 4 also

18   depicts the maximum solar-to-hydrogen conversion efficiency of 18% for a photoelectrochemical

19   water splitting device with a single light-absorber (band gap of 1.96 eV) and with state-of-the-art

20   OER and HER catalysts[38]. The optimal efficiencies for the two processes are comparable when

21   ideal/rapid NO3RR reduction kinetics were assumed because the kinetic overpotentials for the

22   state-of-the-art HER catalysts are much smaller than that for the NO3RR catalysts. With state-of-

23   the-art catalysts, the theoretical limits for the peak nitrogen-removal rates are comparable to the

1   maximum removal rates, of 520 g_N m^{-2} day^{-1}, reported in (bio)electrochemical flow/continuous

2   reactors for ammonia recovery[63].

3   Figure 5 depicts the effect of varying the bulk NO$_3^-$ concentration, $c_{NO_3^-,bulk}$, on the solar-

4   to-chemical efficiency and the rate of nitrogen removal/recovery, while assuming selective

5   NO3RR catalysis to form NH$_3$ (Figure 5(a) and (c)) or N$_2$O (Figure 5(b) and (d)). The bulk

6   concentration of NO$_3^-$ was varied from 0.1 mM to 1000 mM, representing the order-of-magnitude

7   variation in the NO$_3^-$ concentrations corresponding to the EPA limit in drinking water to the

8   presence of NO$_3^-$ in concentrated wastewater sources such as ion-exchange brines (Figure 3).

9   Overall, for any concentration modeled, converting the NO$_3^-$ to N$_2$O, as compared to NH$_3$, results

10 in larger efficiencies and nitrogen removal/recovery rates (12.01% v/s 9.68% at 1000 mM) because

11 of the more effective NO3RR catalysis in the former with Sn-Pt catalysts (**Figure 4**). There is a

12 logarithmic scaling in the maximum efficiencies and the nitrogen removal/recovery rates with the

13 NO$_3^-$ concentration, because of the larger driving force and therefore lower kinetic overpotentials

14 for the electron-transfer reactions (Eq.(12)).

15   For $c_{NO_3^-,bulk}$ = 10, 100 and 1000 mM, the transport of NO$_3^-$ from the bulk solution to the

16 electrode surface does not impact the operating current densities at any band gap of the

17 semiconductor as the mass-transfer limited current density (Eq. (10)) for the NO3RR is much

18 larger than the short-circuit density of the light-absorber. For these concentrations, when the band

19 gaps are smaller than the optimal value, the concentration-dependent NO3RR kinetics limits both

20 the efficiency and nitrogen removal/recovery rates. For the same range of NO$_3^-$ concentration,

21 when the band gaps are larger than 2 eV, the performance is insensitive to changes in the

22 concentration because light-absorption in the semiconductor limits the performance. However, for
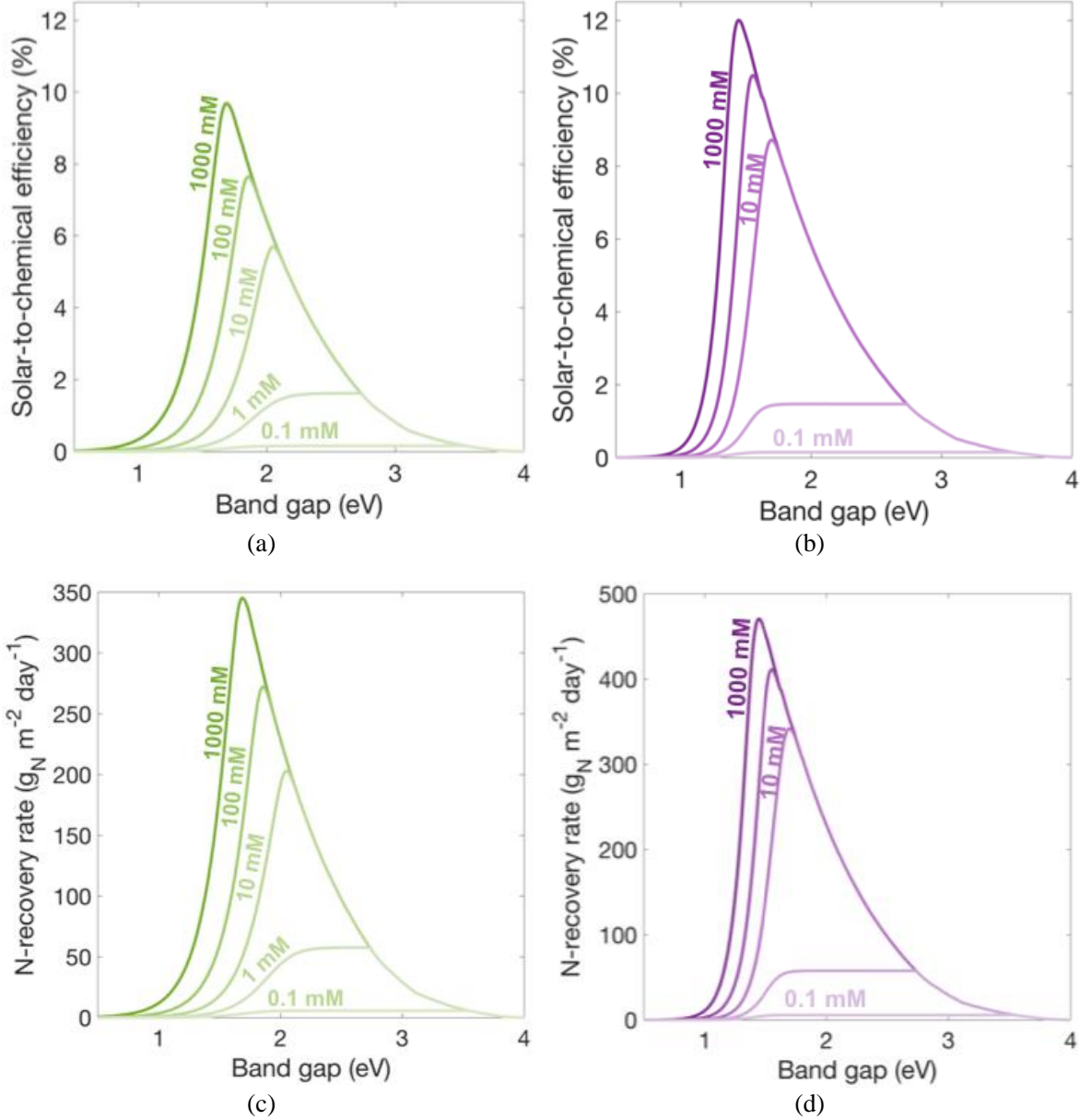
23

Figure 5: Concentration effects on the solar-to-chemical efficiencies ((a) and (b)) and the nitrogen-removal rates ((c) and (d)) with complete selectivity to desired reactions assumed: for (a) and (c), for the NO_3^--to-NH_3 conversion at pH 14, selective OER on IrO_2 and selective NO3RR on Cu was assumed; for (b) and (d), for the NO_3^--to-N_2O conversion at pH 1, selective OER on RuO_2 and selective NO3RR on Sn-Pt was assumed. For all these calculations, a headspace with standard atmospheric conditions (1 atm, 25˚C) with 20.9% of O_2, trace amounts of H_2 (0.5 ppm) and balance N_2 was assumed to determine thermodynamic reaction potentials.

1   the two smaller concentrations, $c_{NO_3^-,bulk} = 0.1$ mM and 1 mM, there is a mass-transfer limited

2   operational regime in addition to the kinetics and light-absorption limited performance. In this

3   regime, there is little-to-no effect of the band gap on the performance, resulting in the *plateau*

18

1   *region* observed in Figure 5(a) and (b). In these conditions, the operating current density of the

2   device (Eq. (4)), is predominantly limited by the rate of diffusion of the reacting NO_3^- species from

3   the bulk electrolyte to the electrocatalyst surface. For NH_3 production, mass-transfer limited

4   efficiencies of 1.62% and 0.16% are predicted for the band gaps of 2.15 – 2.75 eV and 1.65 –

5   2.75 eV, with $c_{NO_3^-,bulk}$ = 1 mM and 0.1 mM respectively. Therefore, the bulk NO_3^- concentration

6   in the waste steam not only has an impact the maximum attainable efficiencies and the nitrogen

7   recovery rates, but also affects how sensitive the performance is to the light-absorber band gaps.

8   Figure 6 reveals the extent to which the competing reactions influences the solar-to-

9   chemical efficiencies. The green and the purple shaded areas (for NH_3 and N_2O respectively)

10   represent the absolute change in efficiency, from assuming selective catalysis to when the *worst-*

11   *case* was modeled for the competing reactions. Four discrete band gaps were selected to represent

12   realistic semiconductor materials for the light absorbers—Si (1 eV), MoS_2 (1.75 eV), $BiVO_4$ (2.5

13   eV), and TiO_2 (3.1 eV). Three bulk NO_3^- concentrations of 1000, 10, and 1 mM were selected to

14   highlight the trends. Consider the results for the NO_3^--to-NH_3 transformation (Figure 6(a)). For all

15   bandgaps, competing reactions results in lower solar-to-chemical efficiencies and nitrogen

16   removal/recovery rates. The peak efficiencies, from Figure 5 are reduced by 9% and 63% for

17   1000 mM and 1 mM NO_3^- respectively. For any band gap, the relative decrease in the efficiency

18   becomes larger when the bulk concentration of NO_3^- becomes smaller (Figure S1 in ESI). This

19   outcome is due to the increase in the NO3RR mass-transfer overpotential with a decrease in the

20   NO_3^- concentration, which in turn increases the driving force for the competing reactions. For the

21   intermediate band gap materials —MoS_2 (1.75 eV) and $BiVO_4$ (2.5 eV) – ORR occurs at the mass-

22   transfer limited current density of ~21 A m^{-2} for all NO_3^- concentrations (blue circles in Figure 6

23   (b)). However, the rate of competing HER increases when the NO_3^- concentration decreases
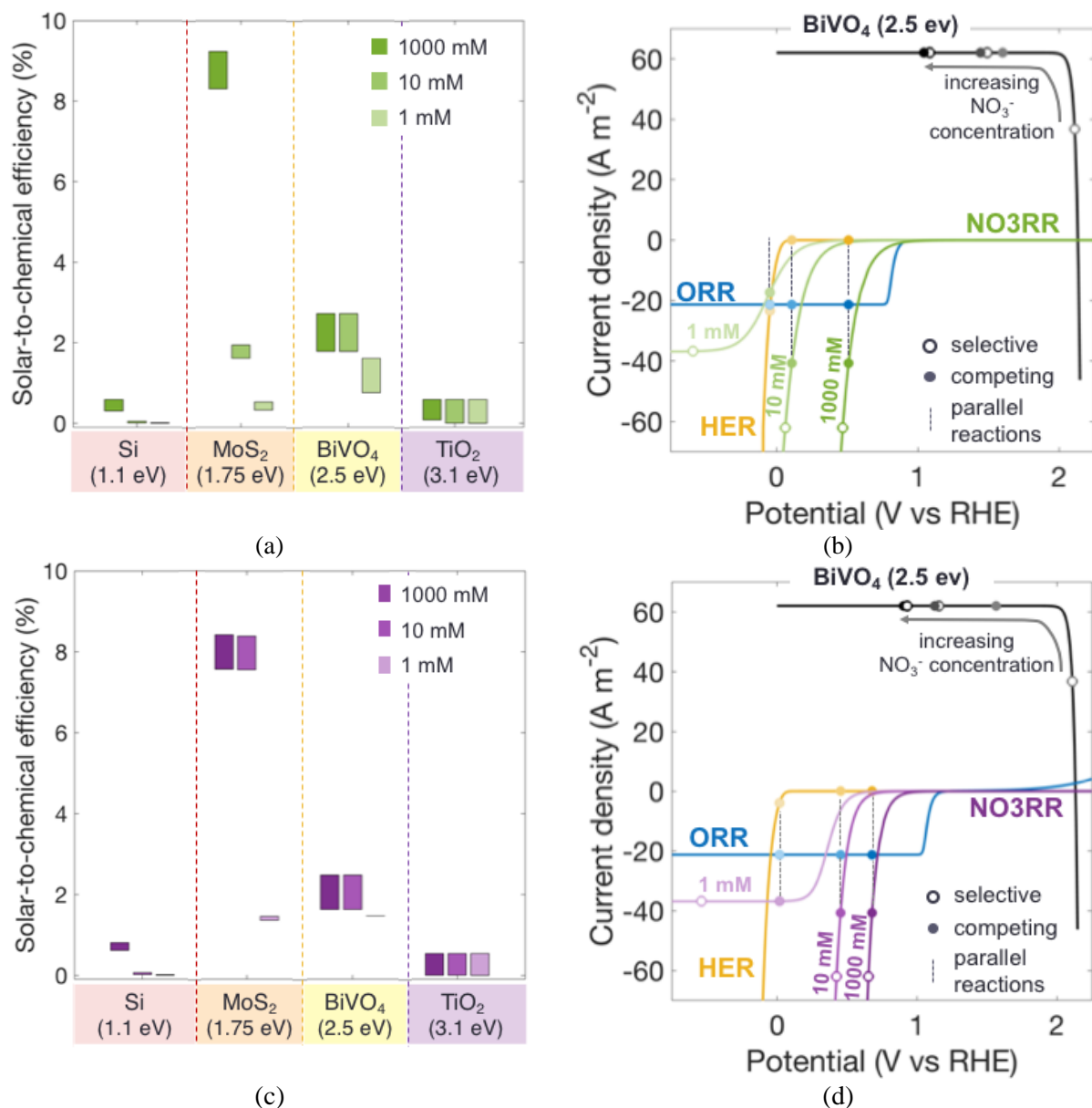
Figure 6: Solar-to-chemical efficiency for (a) NH_3 production and (c) N_2O production when competing HER and ORR reactions are implemented at the cathode with *worst-case* kinetic parameter values (Table 2). (b,d) To further illustrate the driving forces for the competing reactions, the current-voltage behavior for the diode (black) assuming $BiVO_4$ with a band gap of 2.5 eV and the parallel and competing electrochemical reactions at the cathode. Open symbols on the current-voltage plot represent models that assumed selective reactions whereas the filled symbols include the competing reactions. The operating point, j_{op} and V_{op}, is shown on the diode curve (black circles); the cathode potential and current densities for (b) NH_3 production (green) or (d) N_2O production (purple); HER (yellow) ; and ORR (blue).

1

2

1   below 10 mM (yellow circles in Figure 6(b)). For $c_{NO_3^-,bulk} > 1$ mM, mass-transfer limited H_2

2   oxidation occurs instead of H_2 evolution because the cathode potential is larger than the

3   equilibrium potential of H^+/H_2, $V_{cathode} > E_{eq,HER} = 0.19$ V v/s RHE, assuming a head-space with

4   0.5 ppm H_2. For a bulk NO_3^- concentration of 1 mM and a band gap of 2.5 eV, while the NO3RR

5   is mass-transfer limited when selective NO3RR was modeled (open green circles in Figure 6(b)),

6   this limitation ceases to exist when competing reactions were taken into account at the cathode

7   (filled green circles in Figure 6(b)). This trend is also evident in the shift of the operating potential

8   and current densities of the diode (open versus closed black circles) on the diode curve in Figure

9   6(b). For both Si (1.1 eV) and TiO_2 (3.1 eV), the baseline efficiencies without the competing

10 reactions are small due to the lack of driving potential at the cathode for the NO3RR in Si and

11 because of the limited visible light absorption for TiO_2. In both these instances, mass-transfer

12 limited ORR predominates at the cathode as compared to the NO3RR; H_2 oxidation occurs at

13 negligibly small, mass-transfer limited rates of 3.87×10^{-5} A m^{-2}, for all NO_3^- concentrations in

14 the bulk.

15   For the NO_3^--to-N_2O transformation (Figure 6(c)), overall trends are largely similar to what

16 was previously discussed for the NO_3^--to-NH_3 transformation. A subtle difference occurs with

17 respect to the effects of competing HER for the low NO_3^- concentrations (≤ 1 mM). While HER

18 becomes more significant at these NO_3^- concentrations for NH_3 production, it is not the case for

19 N_2O formation because of the lower kinetic potential losses. Therefore, the current onset occurs at

20 a much lower potential on the Sn-Pt catalyst for N_2O formation as compared to the Cu catalyst for

21 NH_3 production. For example, with the $BiVO_4$ light-absorber with a 2.5 eV bandgap, Figure 6(d)

22 reveals that the NO3RR is mass-transfer limited for, both, with and without competing reactions,

23 and therefore the efficiency does not change (Figure 6(c)). The conversion of NO_3^- to N_2O benefits

1 from more efficient catalytic parameters modeled as compared to NH_3, especially at the low NO_3^-

2 concentrations.

3   Overall, even with large driving forces for the competing reactions established by the

4 *worst-case* parameters modeled herein, these results indicate that the competing reactions do not

5 significantly influence the performance (at most 10% relative change in efficiencies and the

6 nitrogen removal/recovery rates) when the NO_3^- concentrations are large ($\geq$ 100 mM) and with

7 optimally selected band gaps. In these cases, the most dominant competing reaction at the cathode

8 is the ORR, which is mass-transfer-limited to current-densities less than 21 A m^{-2}, which is at least

9 five times lesser than the NO3RR current densities.

10
11 **4.3 Comparison with state-of-the-art nitrogen-removal technologies**
12
13   We compared the proposed device with two tertiary technologies that are currently used

14 for nitrogen removal and recovery—(1) electrochemical ammonia stripping[63], and (2) the Sharon-

15 Anammox process that removes NH_3/NH_4^+ contaminants as N_2[61,62]. These three pathways were

16 compared on the basis of the nitrogen-removal rates and the mass-specific energy intensity (Table

17 3). For this comparison, we assumed bulk NO_3^- concentration of 100 mM, state-of-the-art catalysts

18 with perfect selectivity for the NO3RR for NH_3/NH_4^+ production; Figure 6 indicates that the

19 competing reactions do not substantially alter the performance for the 100 mM case. More

20 information about these processes are provided in the ESI (Section 3).

21   For the nitrogen-removal rates, the proposed photoelectrochemical approach achieves

22 nitrogen removal rates comparable to those reported for the electrochemical ammonia-stripping

23 reactors – 272.2 and 411.3 g_N m^{-2} day^{-1} for NH_3 and N_2O production respectively with state-of-

24 the-art catalysts and 100 mM bulk NO_3^- concentration. The Sharon-Anammox is a batch process

25 and thus limited to lower rates of nitrogen removal as compared to the flow reactors, roughly

10 g_N m^{-2} day^{-1} (Section 3 in ESI for calculation details). Therefore, the mass-specific energy intensities were compared at this fixed nitrogen removal rate of 10 g_N m^{-2} day^{-1}. About 10–16 MJ kg_N^{-1} is required by the Sharon-Anammox process, including aeration, pumping and other parasitic power inputs at the plant-scale[61,62]. A specific energy intensity of ~2.4 MJ kg_N^{-1} is estimated, without any consideration of parasitic energy requirements, for the electrochemical ammonia stripping reactor[63]. In comparison, at equivalent nitrogen-removal rates, the energy intensity for the photoelectrochemical approach proposed in this work is 8 MJ kg_N^{-1}, out of which 2.9 MJ kg_N^{-1} is required for the NO_3^-–to–NH_4^+ transformation, 2.6 MJ kg_N^{-1} is estimated for pumping in a flow reactor[98], and an energy requirement of 2.4 MJ kg_N^{-1} was additionally included to recover the NH_3/NH_4^+ formed via electrochemical ammonia stripping. Therefore, the proposed approach has the potential to competitive with one of the most energy-efficient nitrogen-removal technologies with the added dual benefits of harnessing sunlight to treat and remove reactive-nitrogen (NO_3^-) contaminants while also recovering nutrients as NH_3/NH_4^+ (or N_2O).

Table 3: Nitrogen-removal rates and mass-specific energy intensity comparisons for the Sharon-Annamox, electrochemical flow reactor for ammonia stripping and the photoelectrochemical approach discussed in this work.

Metrics (Units)	Nitrogen-removal Technologies		
	Sharon-Anammox	Electrochemical flow reactor for ammonia stripping	Photoelectrochemical device for nitrate-to-ammonia conversion (this work)
Nitrogen-removal rates (g_N m^{-2} day^{-1})	10	384	272.2
Mass-specific energy intensity (MJ kg_N^{-1}) for nitrogen removal at a rate of 10 g_N m^{-2} day^{-1}	10-16	2.4	8

5. Conclusions

In summary, we propose and analyze the performance of a solar-powered wastewater nitrate treatment process that couples water oxidation with nitrate reduction to produce value-

1 added chemicals such as NH_4^+/NH_3 and N_2O. A numerical model was developed to predict the

2 influences of material- and operational- parameters on solar-to-chemical efficiencies and the

3 nitrogen removal/recovery rates. Important modeling innovations were introduced to quantify the

4 influences of reacting species concentrations in the bulk solution and the competing hydrogen

5 evolution and oxygen reduction reactions on the performance. Results reveal that the overall

6 performance of the proposed device is influenced by the combined effects of light absorption in

7 the semiconductor, which was modeled as a function of the band gap; electrocatalytic parameters

8 including the exchange current densities and charge-transfer coefficients for the water oxidation

9 and nitrate reduction reactions; and the species concentrations, which impacted the rates of

10 diffusion of species across the concentration boundary layer.

11   For a bulk NO_3^- concentration of 100 mM, model results predict peak solar-to-chemical

12 efficiencies of 7% and 10%, and nitrogen removal/recovery rates of 260 g_N m^{-2} day^{-1} and

13 395 g_N m^{-2} day^{-1}, for NH_3 and N_2O production with Cu and Sn-Pt catalysts respectively; optimal

14 light-absorber band gaps are 1.89 eV and 1.58 eV respectively. The reacting NO_3^- species

15 concentration impacts the reaction kinetics by influencing the concentration-dependent exchange-

16 current densities and the mass-transfer limited nitrate reduction current densities. For NO_3^-

17 concentrations larger than or equal to 10 mM, efficiencies and the nitrogen removal/recovery rates

18 are limited by the nitrate reduction kinetics or the light-absorber current-voltage behavior.

19 However, for the smaller NO_3^- concentrations, there is a mass-transfer limited operating regime,

20 wherein the efficiencies and the nitrogen removal/recovery rates are unaffected by changes in the

21 light-absorber band gap and the electrocatalytic parameters. In this regime, the operating current

22 densities are only limited by the rate of diffusion of the NO_3^- ions, from the bulk to the surface of

23 the electrocatalyst across a 10-µm thick concentration boundary layer. Competing hydrogen

evolution and oxygen reduction reactions were modeled with *worst-case* parameters deduced from kinetics for these reactions on a Pt-catalyst. For large concentrations (≥ 100 mM) of nitrates and optimally selected light-absorber band gaps, oxygen reduction is the more dominant competing reaction and is mass-transfer limited. Therefore, the peak efficiencies and the nitrogen removal/recovery rates are at most reduced by 11%. The driving force for the hydrogen evolution reaction increases for the smaller NO_3^- concentrations and for increasing light-absorber band gaps.

Model predictions were used to identify light-absorber materials, based on the calculated effects of their band gaps, for NH_3 and N_2O production. For example, MoS_2 with a band gap of 1.75 eV can yield high efficiencies and nitrogen removal rates for NO_3^--to-NH_3 conversion, when NO_3^- concentrations are larger than 10mM. When the concentration becomes smaller, even with a larger band gap light-absorber, such as $BiVO_4$ (2.5 eV), the efficiency remains unaffected. Theoretical predictions for the performance of the proposed photoelectrochemical device in attractive when compared with the state-of-the-art nitrogen removal technologies. A comparative analysis revealed that the nitrogen removal rate and the energy intensity of nitrogen-removal are competitive with reported estimates for electrochemical ammonia stripping and the Sharon-Anammox process.

On the whole, theoretical analyses in this study indicate that transforming wastewater nitrates to value-added chemicals, including NH_3 and N_2O, by utilizing sunlight can be a promising new approach to achieve resource recovery in tertiary wastewater treatment technologies. Future investigations will focus on experimental measurements to further build on this work and to assess the performance of the catalysts and semiconductor materials identified in this work.

Acknowledgments

References

1.   Rockström, J. *et al.* A safe operating space for humanity. *Nature* **461**, 472–475 (2009).

2.   Gao, H., Scherson, Y. D. & Wells, G. F. Towards energy neutral wastewater treatment: methodology and state of the art. *Environ. Sci. Process. Impacts* **16**, 1223–1246 (2014).

3.   Duca, M. & Koper, M. T. M. Powering denitrification: the perspectives of electrocatalytic nitrate reduction. *Energy Environ. Sci.* **5**, 9726 (2012).

4.   Falkowski, P. *et al.* The Global Carbon Cycle : A Test of Our Knowledge of Earth as a System. *Science (80-.).* **290**, 291–297 (2000).

5.   Kapoor, A. & Viraraghavan, T. Nitrate Removal From Drinking Water—Review. *J. Environ. Eng.* **123**, 371–380 (1997).

6.   Heisler, J. *et al.* Eutrophication and harmful algal blooms: A scientific consensus. *Harmful Algae* **8**, 3–13 (2008).

7.   Terblanche, A. P. S. Health hazards of nitrate in drinking water. *Water SA* vol. 17 77–82 (1991).

8.   Gruber, N. & Galloway, J. N. An Earth-system perspective of the global nitrogen cycle. *Nature* **451**, 293–296 (2008).

9.   Scherson, Y. D. *et al.* Nitrogen removal with energy recovery through N2O decomposition. *Energy Environ. Sci.* **6**, 241–248 (2013).

10. Schreiber, F., Wunderlin, P., Udert, K. M. & Wells, G. F. Nitric oxide and nitrous oxide turnover in natural and engineered microbial communities: biological pathways, chemical reactions, and novel technologies. *Front. Microbiol.* **3**, 1–24 (2012).

11. National Research Council. Municipal Wastewater, Sewage Sludge, and Agriculture. in *Use of Reclaimed Water and Sludge in Food Crop Production* 17–45 (The National Academies Press, 1996).

12. Puyol, D. *et al.* Resource recovery from wastewater by biological technologies: Opportunities, challenges, and prospects. *Front. Microbiol.* **7**, 1–23 (2017).

13. Huo, X., Vanneste, J., Cath, T. Y. & Strathmann, T. J. A hybrid catalytic hydrogenation/membrane distillation process for nitrogen resource recovery from nitrate-contaminated waste ion exchange brine. *Water Res.* **175**, 115688 (2020).

14. Liu, J., Choe, J. K., Sasnow, Z., Werth, C. J. & Strathmann, T. J. Application of a Re-Pd bimetallic catalyst for treatment of perchlorate in waste ion-exchange regenerant brine. *Water Res.* **47**, 91–101 (2013).

15. Van Ginkel, S. W., Tang, Y. & Rittmann, B. E. Impact of precipitation on the treatment of real ion-exchange brine using the H2-based membrane biofilm reactor. *Water Sci. Technol.* **63**, 1453–1458 (2011).

16. Yang, T., Doudrick, K. & Westerhoff, P. Photocatalytic reduction of nitrate using titanium dioxide for regeneration of ion exchange brine. *Water Res.* **47**, 1299–1307 (2013).

17. Nichols, K. M., Miles-Richardson, S. R., Snyder, E. M. & Giesy, J. P. Effects of exposure to municipal wastewater in situ on the reproductive physiology of the fathead minnow (Pimephales promelas). *Environ. Toxicol. Chem.* **18**, 2001–2012 (1999).

18. Odjadjare, E. E. O. & Okoh, A. I. Physicochemical quality of an urban municipal wastewater effluent and its impact on the receiving environment. *Environ. Monit. Assess.* **170**, 383–394 (2010).

19. Katz, B. G., Griffin, D. W. & Davis, J. H. Groundwater quality impacts from the land application of treated municipal wastewater in a large karstic spring basin: Chemical and microbiological indicators. *Sci. Total Environ.* **407**, 2872–2886 (2009).

20. S. Pabi L. Reekie, Amarnath, A., Goldstein, R. & Reekie, L. Electricity Use and Management in the Municipal Water Supply and Wastewater Industries. *Epri* 1–194 (2013).

21. United States Environmental Protection Agency. Case Studies on Implementing Low-Cost Modifications to Improve Nutrient Reduction at Wastewater Treatment Plants. *United States Environ. Prot. Agency, Off. Wetl. Ocean. Watersheds, Off. Sci. Technol. Off. Wastewater Manag.* 22 (2015).

22. U.S. Environmental Protection Agency. *Energy Efficiency in Water and Wastewater Facilities: A Guide to Developing and Implementing Greenhouse Gas Reduction Programs*. (2013).

23. Rosca, V., Duca, M., de Groot, M. T. & Koper, M. T. M. Nitrogen Cycle Electrocatalysis. *Chem. Rev.* **109**, 2209–2244 (2009).

24. Dahab, M. F. Nitrate Treatment Methods: An Overview. in *Nitrate Contamination: Exposure, Consequence, and Control* (eds. Bogardi, I. & Kuzelka, R. D.) 351–369 (NATO ASI Series, 1991).

25. Lehman, S. G., Badruzzaman, M., Adham, S., Roberts, D. J. & Clifford, D. A. Perchlorate and nitrate treatment by ion exchange integrated with biological brine treatment. *Water Res.* **42**, 969–976 (2008).

26. Clifford, D., Lin, C.-C., Horng, L.-L. & Boegel, J. *Nitrate Removal from Drinking Water in Glendale, Arizona*. (1987).

27. Kneifel, K., Lührs, G. & Wagner, H. Nitrate Removal by Electrodialysis for Brewing Water. *Desalination* **68**, 203–209 (1988).

28. Bohdziewicz, J., Bodzek, M. & Wąsik, E. The application of reverse osmosis and nanofiltration to the removal of nitrates from groundwater. *Desalination* **121**, 139–147 (1999).

29. Shaffer, D. L., Yip, N. Y., Gilron, J. & Elimelech, M. Seawater desalination for agriculture by integrated forward and reverse osmosis: Improved product water quality for potentially less energy. *J. Memb. Sci.* **415**–**416**, 1–8 (2012).

30. Samatya, S., Kabay, N., Yüksel, Ü., Arda, M. & Yüksel, M. Removal of nitrate from aqueous solution by nitrate selective ion exchange resins. *React. Funct. Polym.* **66**, 1206–1214 (2006).

31. Shaner, M. R., Fountaine, K. T. & Lewerenz, H.-J. Current-voltage characteristics of coupled photodiode-electrocatalyst devices. *Appl. Phys. Lett.* **103**, 143905 (2013).

32. Winkler, M. T., Cox, C. R., Nocera, D. G. & Buonassisi, T. Modeling integrated photovoltaic – electrochemical devices using steady-state equivalent circuits. *Natl. Acad. Sci.* (2013) doi:10.1073/pnas.1301532110.

33. Bala Chandran, R., Breen, S., Shao, Y., Ardo, S. & Weber, A. Z. Evaluating particle-suspension reactor designs for Z-scheme solar water splitting via transport and kinetic modeling. *Energy Environ. Sci.* **11**, 115–135 (2018).

34. Keene, S., Bala Chandran, R. & Ardo, S. Calculations of theoretical efficiencies for electrochemically-mediated tandem solar water splitting as a function of bandgap energies and redox shuttle potential. *Energy Environ. Sci.* **12**, 261–272 (2019).

35. Fountaine, K. T., Lewerenz, H. J. & Atwater, H. A. Efficiency limits for photoelectrochemical water-splitting. *Nat. Commun.* **7**, 13706 (2016).

36. Shockley, W. & Queisser, H. J. Detailed Balance Limit of Efficiency of p-n Junction Solar Cells. *J. Appl. Phys.* **32**, 510–519 (1961).

37. Xiang, C. *et al.* Modeling, Simulation, and Implementation of Solar-Driven Water-Splitting Devices. *Angew. Chemie Int. Ed.* **55**, 12974–12988 (2016).

38. Hu, S., Xiang, C., Haussener, S., Berger, A. D. & Lewis, N. S. An analysis of the optimal band gaps of light absorbers in integrated tandem photoelectrochemical water-splitting systems. *Energy Environ. Sci.* **6**, 2984 (2013).

39. Wang, Q., Hisatomi, T., Ma, S. S. K., Li, Y. & Domen, K. Core/shell structured La- and Rh-Codoped SrTiO3 as a hydrogen evolution photocatalyst in Z-scheme overall water splitting under visible light irradiation. *Chem. Mater.* **26**, 4144–4150 (2014).

40. McCrory, C. C. L., Jung, S., Peters, J. C. & Jaramillo, T. F. Benchmarking Heterogeneous Electrocatalysts for the Oxygen Evolution Reaction. *J. Am. Chem. Soc.* **135**, 16977–16987 (2013).

41. Jung, S., McCrory, C. C. L., Ferrer, I. M., Peters, J. C. & Jaramillo, T. F. Benchmarking nanoparticulate metal oxide electrocatalysts for the alkaline water oxidation reaction. *J. Mater. Chem. A* **4**, 3068–3076 (2016).

42. McCrory, C. C. L. *et al.* Benchmarking Hydrogen Evolving Reaction and Oxygen Evolving Reaction Electrocatalysts for Solar Water Splitting Devices. *J. Am. Chem. Soc.* **137**, 4347–4357 (2015).

43. Tugaoen, H. O., Garcia-Segura, S., Hristovski, K. & Westerhoff, P. Challenges in photocatalytic reduction of nitrate as a water treatment technology. *Sci. Total Environ.* **599**–**600**, 1524–1551 (2017).

44. Wehbe, N. *et al.* Comparative study of photocatalytic and non-photocatalytic reduction of nitrates in water. *Appl. Catal. A Gen.* **368**, 1–8 (2009).

45. Marks, R., Yang, T., Westerhoff, P. & Doudrick, K. Comparative analysis of the photocatalytic reduction of drinking water oxoanions using titanium dioxide. *Water Res.* **104**, 11–19 (2016).

46. Loeb, S. K. *et al.* The Technology Horizon for Photocatalytic Water Treatment: Sunrise or Sunset? *Environ. Sci. Technol.* **53**, 2937–2947 (2019).

47. Garcia-Segura, S., Lanzarini-Lopes, M., Hristovski, K. & Westerhoff, P. Electrocatalytic reduction of nitrate: Fundamentals to full-scale water treatment applications. *Appl. Catal. B Environ.* **236**, 546–568 (2018).

48. Barrabés, N. & Sá, J. Catalytic nitrate removal from water, past, present and future perspectives. *Appl. Catal. B Environ.* **104**, 1–5 (2011).

49. Yang, J., Calle-Vallejo, F., Duca, M. & Koper, M. T. M. Electrocatalytic reduction of nitrate on a Pt electrode modified by p-block metal adatoms in acid solution. *ChemCatChem* **5**, 1773–1783 (2013).

50. Chen, T., Li, H., Ma, H. & Koper, M. T. M. Surface Modi fi cation of Pt (100) for Electrocatalytic Nitrate Reduction to Dinitrogen in Alkaline Solution. **2**, (2015).

51. Gootzen, J. F. E., Lefferts, L. & van Veen, J. A. R. Electrocatalytic nitrate reduction on palladium based catalysts activated with germanium. *Appl. Catal. A Gen.* **188**, 127–136 (1999).

52. Martínez, J., Ortiz, A. & Ortiz, I. Environmental State-of-the-art and perspectives of the catalytic and electrocatalytic reduction of aqueous nitrates. *"Applied Catal. B, Environ.* **207**, 42–59 (2017).

53. Dortsiou, M., Katsounaros, I., Polatides, C. & Kyriacou, G. Electrochemical removal of nitrate from the spent regenerant solution of the ion exchange. *Desalination* **248**, 923–930 (2009).

54. Bergmann, H., Bouzek, K., Paidar, M. & Sadiâlkova, a. Electrochemical reduction of nitrate in weakly alkaline solutions. *J. Appl. Electrochem.* **31**, 1185–1193 (2001).

55. Kuang, P., Natsui, K. & Einaga, Y. Comparison of performance between boron-doped diamond and copper electrodes for selective nitrogen gas formation by the electrochemical reduction of nitrate. *Chemosphere* **210**, 524–530 (2018).

56. Cattarin, S. Electrochemical reduction of nitrogen oxyanions in 1 M sodium hydroxide solutions at silver, copper and CuInSe2 electrodes. *J. Appl. Electrochem.* **22**, 1077–1081 (1992).

57. Reyter, D., Bélanger, D. & Roué, L. Study of the electroreduction of nitrate on copper in alkaline solution. *Electrochim. Acta* **53**, 5977–5984 (2008).

58. Yang, J., Duca, M., Schouten, K. J. P. & Koper, M. T. M. Formation of volatile products during nitrate reduction on a Sn-modified Pt electrode in acid solution. *J. Electroanal. Chem.* **662**, 87–92 (2011).

59. Katsounaros, I., Ipsakis, D., Polatides, C. & Kyriacou, G. Efficient electrochemical reduction of nitrate to nitrogen on tin cathode at very high cathodic potentials. *Electrochim. Acta* **52**, 1329–1338 (2006).

60. Genders, J. D., Hartsough, D. & Hobbs, D. T. Electrochemical reduction of nitrates and nitrites in alkaline nuclear waste solutions. *J. Appl. Electrochem.* **26**, 1–9 (1996).

61. Lackner, S. *et al.* Full-scale partial nitritation/anammox experiences - An application survey. *Water Res.* **55**, 292–303 (2014).

62. Maurer, M., Schwegler, P. & Larsen, T. A. Nutrients in urine: Energetic aspects of removal and recovery. *Water Sci. Technol.* **48**, 37–46 (2003).

63. Kuntke, P. *et al.* (Bio)electrochemical ammonia recovery: progress and perspectives. *Appl. Microbiol. Biotechnol.* **102**, 3865–3878 (2018).

64. Zamfirescu, C. & Dincer, I. Using ammonia as a sustainable fuel. **185**, 459–465 (2008).

65. Lan, R. & Tao, S. Ammonia as a Suitable Fuel for Fuel Cells. *Front. Energy Res.* **2**, 35 (2014).

66. Afif, A. *et al.* Ammonia-fed fuel cells: A comprehensive review. *Renew. Sustain. Energy Rev.* **60**, 822–835 (2016).

67. Scherson, Y. D. *et al.* Nitrogen removal with energy recovery through N 2 O decomposition. *Energy Environ. Sci.* **6**, 241–248 (2013).

68. Parmon, V. N., Panov, G. I., Uriarte, A. & Noskov, A. S. Nitrous oxide in oxidation chemistry and catalysis: application and production. *Catal. Today* **100**, 115–131 (2005).

69. Plieth, W. J. Nitrogen. in *Encyclopedia of Electrochemistry of the Elements, Vol. VIII* (ed. Bard, A. J.) 321–479 (Marcel Dekker, Inc., 1978).

70. Singh, N. & Goldsmith, B. R. Role of Electrocatalysis in the Remediation of Water Pollutants. *ACS Catal.* 3365–3371 (2020) doi:10.1021/acscatal.9b04167.

71. Lide, D. R. Standard Thermodynamic Properties of Chemical Substances. in *CRC Handbook of Chemistry and Physics* (ed. David R. Lide) 5–22 (CRC Press, 2005).

72. Reyter, D. *et al.* Nitrate removal by a paired electrolysis on copper and Ti/IrO2 coupled electrodes - Influence of the anode/cathode surface area ratio. *Water Res.* **44**, 1918–1926 (2010).

73. Deng, J. *et al.* Nanowire Photoelectrochemistry. *Chem. Rev.* **119**, 9221–9259 (2019).

74. Bard, A. J. & Faulkner, L. R. *Electrochemical Methods Fundamentals and Applications*. (John Wiley & Sons, Inc., 2001).

75. Chang, C. & Wen, T. Kinetics of Oxygen Reduction at IrO2-Coated Titanium Electrode in

Alkaline Solution. *J. Electrochem. Soc.* **143**, 1485–1491 (1996).

76. Sheng, W., Gasteiger, H. A. & Shao-Horn, Y. Hydrogen Oxidation and Evolution Reaction Kinetics on Platinum: Acid vs Alkaline Electrolytes. *J. Electrochem. Soc.* **157**, B1529 (2010).

77. Sheng, W., Myint, M., Chen, J. G. & Yan, Y. Correlating the hydrogen evolution reaction activity in alkaline electrolytes with the hydrogen binding energy on monometallic surfaces. *Energy Environ. Sci.* **6**, 1509–1512 (2013).

78. Macia, M. D., Campina, J. M., Herrero, E. & Feliu, J. M. On the kinetics of oxygen reduction on platinum stepped surfaces in acidic media. *J. Electroanal. Chem.* **564**, 141–150 (2004).

79. Dong, Q., Santhanagopalan, S. & White, R. E. Simulation of the Oxygen Reduction Reaction at an RDE in 0 . 5 M H 2 SO 4 Including an Adsorption Mechanism. **154**, (2007).

80. Kuzume, A., Herrero, E. & Feliu, J. M. Oxygen reduction on stepped platinum surfaces in acidic media. **599**, 333–343 (2007).

81. Geniès, L., Faure, R. & Durand, R. Electrochemical reduction of oxygen on platinum nanoparticles in alkaline media. *Electrochim. Acta* **44**, 1317–1327 (1998).

82. Reyter, D., Chamoulaud, G., Bélanger, D. & Roué, L. Electrocatalytic reduction of nitrate on copper electrodes prepared by high-energy ball milling. *J. Electroanal. Chem.* **596**, 13–24 (2006).

83. Mattarozzi, L. *et al.* Electrochemical reduction of nitrate and nitrite in alkaline media at CuNi alloy electrodes. *Electrochim. Acta* **89**, 488–496 (2013).

84. Pentland, N., Bockris, J. O. & Sheldon, E. Hydrogen Evolution Reaction on Copper, Gold, Molybdenum, Palladium, Rhodium, and Iron. *J. Electrochem. Soc.* **104**, 182 (1957).

85. MathWorks. Symbolic Math Toolbox ™ User's Guide 2018a. 1714–1724 (2018).

86. Hirakawa, H., Hashimoto, M., Shiraishi, Y. & Hirai, T. Photocatalytic Conversion of Nitrogen to Ammonia with Water on Surface Oxygen Vacancies of Titanium Dioxide. *J. Am. Chem. Soc.* **139**, 10929–10936 (2017).

87. Suryanto, B. H. R. *et al.* Challenges and prospects in the catalysis of electroreduction of nitrogen to ammonia. *Nat. Catal.* **2**, 290–296 (2019).

88. Sawyer, C. N., McCarty, P. L. & Parkin, G. F. *Chemistry for environmental engineering and science.* (2003).

89. U.S. Environmental Protection Agency. *2018 Edition of the Drinking Water Standards and Health Advisories Tables*. (2018).

90. U.S. EPA. *Technical Development Document for the Effluent Limitations Guidelines and Standards for the Oil and Gas Extraction Point Source Category. United States Environmental Protection Agency* vol. EPA-820-R- (2016).

91. U.S. Environmental Protection Agency & US EPA. Development document for final effluent limitations guidelines and standards for the iron and steel manufacturing point source category. 1062 (2002).

92. U.S. Environmental Protection Agency. Industrial Wastewater Treatment Technologies Database.

93. Prasad, S., Weidner, J. W. & Farell, A. E. A Boundary-Layer Model of A Parallel-Plate Electrochemical Reactor Model for the Destruction of Nitrate and Nitrite in Alkaline Waste Solutions. *J. Electrochem. Soc.* **142**, 1152–1161 (1995).

94. Moreno, C., Farahbakhshazad, N. & Morrison, G. M. Ammonia removal from oil refinery

effluent in vertical upflow macrophyte column systems. *Water. Air. Soil Pollut.* **135**, 237–247 (2002).

95. Ghasemi, Z., Younesi, H. & Zinatizadeh, A. A. Preparation, characterization and photocatalytic application of TiO2/Fe-ZSM-5 nanocomposite for the treatment of petroleum refinery wastewater: Optimization of process parameters by response surface methodology. *Chemosphere* **159**, 552–564 (2016).

96. Abdel Wahaab, R. & Alseroury, F. A. Wastewater treatment: a case study of electronics manufacturing industry. *Int. J. Environ. Sci. Technol.* **16**, 47–58 (2019).

97. Hasebe, Y. *et al.* High-rate nitrification of electronic industry wastewater by using nitrifying granules. *Water Sci. Technol.* **76**, 3171–3180 (2017).

98. Garcia-Rodriguez, O. *et al.* Mineralization of electronic wastewater by electro-Fenton with an enhanced graphene-based gas diffusion cathode. *Electrochim. Acta* **276**, 12–20 (2018).

99. Mousset, E., Wang, Z., Olvera-Vargas, H. & Lefebvre, O. Advanced electrocatalytic pre-treatment to improve the biodegradability of real wastewater from the electronics industry — A detailed investigation study. *J. Hazard. Mater.* **360**, 552–559 (2018).

100. Shivaraman, N. *et al.* A two-stage biological treatment system for ammonium-nitrate-laden wastewater. *World J. Microbiol. Biotechnol.* **17**, 447–453 (2001).

101. Maine, M. A. *et al.* Hybrid constructed wetlands for the treatment of wastewater from a fertilizer manufacturing plant: Microcosms and field scale experiments. *Sci. Total Environ.* **650**, 297–302 (2019).

102. Jianping, W., Xiaoqiang, J., Lei, P., Changlin, W. & Guozhu, M. Nitrifying treatment of wastewater from fertilizer production in a multiple airlift loop bioreactor. *Biochem. Eng. J.* **25**, 33–37 (2005).

103. Jianping, W., Wei, P. L. H., Liping, D. & Guozhu, M. The denitrification of nitrate contained wastewater in a gas-liquid-solid three-phase flow airlift loop bioreactor. *Biochem. Eng. J.* **15**, 153–157 (2003).

104. Akyol, A., Can, O. T., Demirbas, E. & Kobya, M. A comparative study of electrocoagulation and electro-Fenton for treatment of wastewater from liquid organic fertilizer plant. *Sep. Purif. Technol.* **112**, 11–19 (2013).

105. Gabaldon, C. *et al.* Biological nitrate removal from wastewater of a metal-finishing industry. **148**, 485–490 (2007).

106. Bockris, J. O. Electrochemical Reductions of Hg(II), Ruthenium-Nitrosyl Complex, Chromate, and Nitrate in a Strong Alkaline Solution. *J. Electrochem. Soc.* **143**, 3801 (1996).

Electronic Supplementary Information

Harnessing Photoelectrochemistry for Wastewater Nitrate Treatment Coupled with Resource Recovery

Luisa Barrera[1] and Rohini Bala Chandran[1*]

[1] Department of Mechanical Engineering, 2350 Hayward St., G. G. Brown Building, University of Michigan, Ann Arbor, MI 48109

* Corresponding author: rbchan@umich.edu

1. Nomenclature

Symbols	
a	activity of modeled aqueous/dissolved species, unitless with $a_{O/R} = \dfrac{c_{O/R}}{c_{O/R,ref}}$
c	speed of light, 3.0×10^8 m s^{-1}
C	concentration of modeled species, mol m^{-3}
D	diffusion coefficient of modeled species, m^2 s^{-1}
E^0	standard electrochemical potential, V vs NHE
E_g	band gap of the semiconductor material, eV
E_{eq}	Nernst potential, V
E_N	specific energy intensity, MJ kg$_N^{-1}$
F	Faraday's constant, 96485 C mol^{-1}
Δg^0	standard state free energy change associated with a reaction, kJ mol^{-1}
h	Planck constant, 6.626×10^{-34} J s
j	current density, A m^{-2}
j_0	exchange current density, A m^{-2}
k_B	Boltzmann constant, 1.38×10^{-23} J K^{-1}
m_N	molar mass of nitrogen, 14 g$_N$ mol^{-1} or 0.014 kg$_N$ mol^{-1}
n_d	ideality factor of the diode, here assumed to be 1
n_e	number of electrons exchanged during reaction
R_N	nitrogen-removal rate, g$_N$ m^{-2} day^{-1}
q_e	elementary charge, 1.6021×10^{-19} C
$\dot{r}$	molar flux, mol m^{-2} s^{-1}
R	gas constant, 8.314 J K^{-1} mol^{-1}
T	ambient temperature, 298.15 K (here, also the diode temperature)
t_{day}	number of seconds in a day, 86400 s day^{-1}
V	potential, V

Greek	
α	charge-transfer coefficient
δ_{BL}	boundary-layer thickness, μm
η	kinetic overpotential, mV
$\eta_{solar-to-chemical}$	solar-to-chemical efficiency, %
υ	photon frequency, s^{-1}
ν	stoichiometric coefficient for modeled reactions
ϕ	frequency-dependent photon flux, s^{-1} m^{-2}

Subscripts	
a	pertinent to the anode
bulk	pertinent to species concentration
c	pertinent to the cathode
g	indicating the min. frequency of photons that can be absorbed by the diode
i	pertinent to the reaction modeled
k	pertinent to the kinetic overpotential
l	pertinent to the limiting current density
mt	pertinent to the mass-transport overpotential

O	pertinent to the oxidized species
op	pertinent to the operating current density and potential of the device
R	pertinent to the reduced species
ref	pertinent to the reference value from the literature
rr	pertinent to the radiation recombination current density
sc	pertinent to the short-circuit current density
solar	pertinent to the incident solar spectrum
tot	total

Other

AM1.5	air mass 1.5 reference spectrum for terrestrial solar insolation
BOD	biological oxygen demand, $mg\text{-}O_2/L$
e^-/h^+	electron/hole pair
EPA	U.S. Environmental Protection Agency
HER	hydrogen evolution reaction
NO3RR	nitrate reduction reaction
OER	oxygen evolution reaction
ORR	oxygen reduction reaction
R1	net reaction 1, where nitrates are converted to ammonia
R2	net reaction 2, where nitrates are converted to nitrous oxide
R3	net reaction 3, where nitrates are converted to nitrogen
RE	relative difference
RHE	reversible hydrogen electrode, used as a reference
~	on the same order of magnitude

2. Solar-to-Chemical Efficiencies and Nitrogen Removal/Recovery Rates

Figure S1 shows the relative difference (RE) for the solar-to-chemical efficiency was calculated by comparing the efficiencies with, $\eta_{solar-to-chemical,comp}$, and without, $\eta_{solar-to-chemical,no\ comp}$, competing reactions as function of the bulk NO_3^- concentration. Both HER and ORR were implemented with "*worst-case*" kinetic parameters. An increase in this relative difference corresponds to an increase in the effect of the competing reactions; a value of 100% implies that the efficiency value with competing reactions approached 0. On Figure S1(a), the relative difference decreases with increasing concentration for all band gaps, with the largest values overall reached by TiO_2 and Si. For the formation of N_2O, on Figure 1(b), the smaller concentrations show less of an effect due to the competing reactions, which follows from the mass-transport limited behavior of the NO3RR shown on Figure 6.

$$RE(\%) = \frac{\eta_{solar-to-chemical,no\ comp} - \eta_{solar-to-chemical,comp}}{\eta_{solar-to-chemical,no\ comp}} \tag{S1}$$
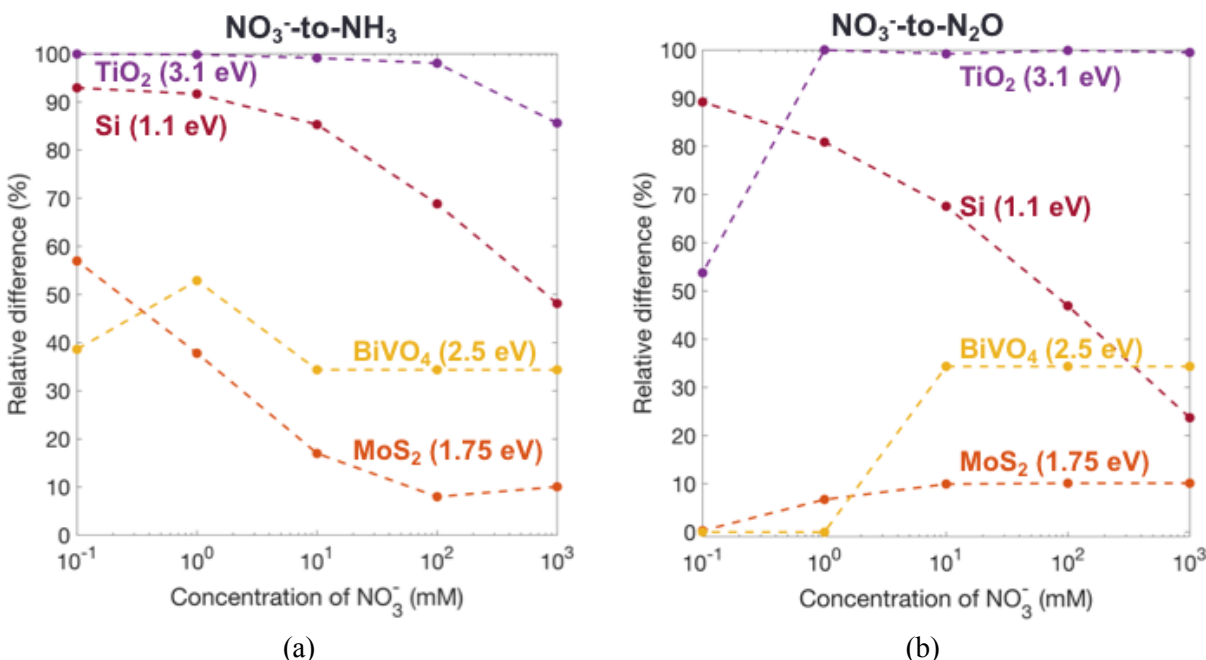

Figure S1: Relative decrease (%) as a function of NO_3^- concentration for Si (red), MoS_2 (orange), $BiVO_4$ (yellow) and TiO_2 (purple) as discussed in Figure 6 for the (a) NO_3^--to-NH_3 transformation and (b) NO_3^--to-N_2O transformation

3. Comparison with state-of-the-art nitrogen-removal technologies

The ammonia stripping reactor recovers NH_3/NH_4^+ nutrients that are present in the solution in an electrochemical flow cell by applying an electric field[1]. This approach offers the advantages of high nitrogen-recovery rates, up to 384 g_N m^{-2} day^{-1}, because of improved mass-transport in flow reactors[1]. However, it relies on the presence of NH_3/NH_4^+ in the waste stream, unlike our device that transforms the NO_3- to NH_3 or N_2O already.

The Sharon-Anammox process is an energy-efficient, biological pathway to transform reactive-nitrogen contaminants present in the form of NH_3/NH_4^+ to N_2 [2]. However, with this approach the nutrients in wastewater are not recovered but lost as N_2. Because this process is typically carried out in batch-reactors, volumetric nitrogen-removal rates of up to 2 kg_N m^{-3} day^{-1} have been reported[3,4]. To translate the volumetric rate to an aerial rate, a biofilm/membrane specific surface area of ~200 m^{-2} m^{-3} was assumed[5], which results in an areal rate of approximately 10 g_N m^{-2} day^{-1}.

References:
1. Kuntke, P. *et al.* (Bio) electrochemical ammonia recovery : progress and perspectives. *Appl. Microbiol. Biotechnol.* **2**, 3865–3878 (2018).
2. Dongen, L. G. J. . van, Jetten, M. S. M. & Loosdrecht, M. C. M. van. *The Combined Sharon/Anammox Process: A sustainable method for N-removal from sludge water.* (2001).
3. Lackner, S. *et al.* Full-scale partial nitritation/anammox experiences - An application survey. *Water Res.* **55**, 292–303 (2014).
4. Maurer, M., Schwegler, P. & Larsen, T. A. Nutrients in urine: Energetic aspects of removal and recovery. *Water Sci. Technol.* **48**, 37–46 (2003).
5. Xie, G. J., Cai, C., Hu, S. & Yuan, Z. Complete nitrogen removal from synthetic anaerobic sludge digestion liquor through integrating anammox and denitrifying anaerobic methane oxidation in a membrane biofilm reactor. *Environ. Sci. Technol.* **51**, 819–827 (2017).